PHYSICAL REVIEW B **88**, 174408 (2013)

Diluted antiferromagnets in a field seem to be in a different universality class than the random-field Ising model

Björn Ahrens,[1,2] Jianping Xiao,[1] Alexander K. Hartmann,[2] and Helmut G. Katzgraber[1,3,4]
[1]*Department of Physics and Astronomy, Texas A&M University, College Station, Texas 77843-4242, USA*
[2]*Institut für Physik, Carl-von-Ossietzky Universität, 26111 Oldenburg, Germany*
[3]*Materials Science and Engineering Program, Texas A&M University, College Station, Texas 77843-3003, USA*
[4]*Theoretische Physik, ETH Zurich, CH-8093 Zurich, Switzerland*

(Received 11 February 2013; published 13 November 2013)

We perform large-scale Monte Carlo simulations using the Machta-Newman-Chayes algorithms to study the critical behavior of both the diluted antiferromagnet in a field with 30% dilution and the random-field Ising model with Gaussian random fields for different field strengths. Analytical calculations by Cardy [Phys. Rev. B **29**, 505 (1984)] predict that both models map onto each other and share the same universality class in the limit of vanishing fields. However, a detailed finite-size scaling analysis of the Binder cumulant, the two-point finite-size correlation length, and the susceptibility suggests that even in the limit of small fields, where the mapping is expected to work, both models are not in the same universality class. Based on our numerical data, we present analytical expressions for the phase boundaries of both models.

DOI: 10.1103/PhysRevB.88.174408 PACS number(s): 64.60.De, 75.10.Nr, 75.40.−s, 75.50.Lk

I. INTRODUCTION

The random-field Ising model[1] (RFIM) is of paramount importance in the field of disordered systems.[2–5] A plethora of problems across disciplines can be studied via the RFIM, ranging from the thermodynamics of disordered magnets,[6] hysteresis in magnetic systems and Barkhausen noise,[7–9] tunable domain-wall pinning,[10] the random pinning of polymers,[11] and even water seepage in porous media. As such, the RFIM is still under intense theoretical, as well as numerical and experimental scrutiny.

More recently, the RFIM has been realized in diluted dipolar magnets in a transverse field such as $\mathrm{LiHo_xY_{1-x}F_4}$. However, most experimental studies focus on diluted antiferromagnets in a field (DAFF), such as $\mathrm{Fe_xZn_{1-x}F_2}$.[3,12–15] Fishman and Aharony[16] were the first to note that a random antiferromagnet in a field can be described by the RFIM, and Cardy[17] predicted, using a mean-field argument, that the critical behavior of both models should be in the same universality class in the limit of small fields. The work of Fishman and Aharony,[16] as well as Cardy,[17] therefore opened the door for intense experimental investigation of the RFIM via DAFF materials. However, early experiments and simulations already hinted towards discrepancies between experimental and numerical estimates of the critical exponents.[3,18,19] On the other hand, exact ground-state calculations using moderate system sizes suggested an agreement between the critical exponents for both models when the random fields are Gaussian distributed, however not when the random fields are drawn from a bimodal distribution.[18,19] This result, however, has been revised recently,[20] i.e., the universality class of the RFIM is independent of the form of the implemented random-field distribution.

In this paper we perform detailed Monte Carlo simulations of both the RFIM and the DAFF. The latter is studied at 30% dilution, i.e., below the percolation threshold for vacancies. Using a finite-size scaling analysis of the Binder cumulant, the two-point finite-size correlation function, and the susceptibility, we show that even in the limit of small fields—where the Cardy mapping[17] is expected to work—both models seem to be in different universality classes. Therefore, care should be taken when making predictions for the critical behavior of the RFIM using experiments on DAFF materials. Finally, we present heuristic analytical expressions based on our numerical data for the phase boundaries of both models to help guide experimental studies.

The manuscript is structured as follows. In Sec. II we introduce both the RFIM and the DAFF, followed by an explanation of the used algorithms in Sec. III, as well as the measured quantities in Sec. IV. In Sec. V we show our numerical results, followed by a detailed discussion of the phase boundaries and universality between both models in Sec. VI.

II. MODELS

The Hamiltonian of the diluted antiferromagnet in a field (DAFF) is given by

$$\mathcal{H}_{\mathrm{DAFF}} = +J\sum_{\langle i,j\rangle}\varepsilon_i\varepsilon_j S_i S_j - B\sum_i \varepsilon_i S_i, \qquad (1)$$

and the Hamiltonian for the random-field Ising model (RFIM) is

$$\mathcal{H}_{\mathrm{RFIM}} = -J\sum_{\langle i,j\rangle} S_i S_j - h\sum_i \delta_i S_i. \qquad (2)$$

In Eqs. (1) and (2) $S_i \in \{\pm 1\}$ represent Ising spins, $J = 1$ is the coupling constant between two adjacent spins, and $\langle i,j\rangle$ denotes a sum over nearest neighbors. The linear term in S_i couples to an external field: For the DAFF it is an externally-applied uniform field B, whereas for the RFIM the spins couple to a random field of strength $h\delta_i$, where the δ_i are quenched random variables chosen from a Gaussian distribution with zero mean and standard deviation unity. This means that the typical field has strength h. In the DAFF $\varepsilon_i \in \{0,1\}$ represents the site dilution, where each site is randomly and independently occupied by a spin ($\varepsilon_i = 1$) with probability p. Here, we fix the dilution to $1 - p = 0.3$. Both models are studied in three space dimensions on a lattice with $N = L^3$ spins, L being the linear size of the lattice.

III. ALGORITHM

The simulations are done using the Machta-Newman-Chayes replica-exchange (MNC) algorithm[21] combined with single-spin Metropolis Monte Carlo.[22,23] The MNC algorithm is a mixture of the Swendsen-Wang exchange algorithm[24] and simulated tempering Monte Carlo.[25,26] Note that the latter is not efficient when simulating random-field systems.[27] The advantage of the MNC algorithm over standard parallel tempering lies in the fact that we can choose any path in the field-temperature plane. Although parallel tempering can also be implemented with a variable field, the method does not perform efficiently when systems have disorder.[28]

In the MNC algorithm[21] a cluster of connected spins is grown between two replicas with the same disorder but at different points in the parameter space, i.e., (T,B) and (T',B'), where T represents the temperature and B the external field (here for the case of the DAFF). Starting from an arbitrary spin with different sign in both realizations, adjacent spins pointing in the same direction are successively added to the cluster with probability

$$p(\beta,\beta') = 1 - \exp\{-2(\beta + \beta')\}, \tag{3}$$

where $\beta = 1/T$ is the inverse temperature. Once no more spins can be added to the cluster $\mathcal{C}$, it flips with the Metropolis probability[29] $\min\{1, \exp(-\Sigma)\}$, where

$$\Sigma_{\mathrm{DAFF}} = 2\,\mathrm{sign}(\mathcal{C})[(\beta - \beta')(n_{++} - n_{--}) + (B - B')|\mathcal{C}|] \tag{4}$$

for the DAFF, and for the RFIM

$$\Sigma_{\mathrm{RFIM}} = 2\,\mathrm{sign}(\mathcal{C})\left[(\beta - \beta')(n_{++} - n_{--}) - (h - h')\sum_{i\in\mathcal{C}}\delta_i\right]. \tag{5}$$

Here $|\mathcal{C}|$ is the number of spins in the cluster, $\mathrm{sign}(\mathcal{C})$ the orientation of the spin in the replica having inverse temperature β, n_{++} and n_{--} are the number of bonds connecting to nearest neighbors of the cluster with spin up and spin down in both replicas, respectively. After each cluster update, $(L/2)^3$ attempts to flip single spins are performed, where L is the linear size of the system.

As stated before, the MNC algorithm enables us to perform simulations along any arbitrary path in parameter space. We denote such path a replica chain (RC). The phase boundaries for the RFIM and DAFF in the field-temperature plane are well described by ellipses (see below). To reduce corrections to finite-size scaling[30,31] we therefore choose paths in the field-temperature plane that cut the phase boundaries at as orthogonal an angle as possible. This means that, in general, $T \sim h$ for the RFIM and $T \sim B$ for the DAFF. To ensure efficient mixing and therefore fast convergence of the Monte Carlo method, we additionally connect the point with the highest field within the disordered phase to another RC that runs parallel to the approximated phase boundary to a temperature $T > T_c$ and $B = 0$ ($h = 0$ for the RFIM), where T_c is the critical temperature of the model at zero field (see Fig. 5, light dashed lines). This end point of the second RC is simulated efficiently by the Wolff cluster algorithm.[32] Simulation parameters are listed in Tables I and II for the RFIM and DAFF, for the first RCs, respectively.

TABLE I. Simulation parameters for the RFIM along different nontrivial paths of the type $h = a + bT$ in the h-T plane for different linear system sizes L (the first two path types have $b = 0$). N_{sa} is the number of disorder realizations. N_T corresponds to the number of temperatures (points) along the simulation path. T_{min} and T_{max} are the lowest and highest temperature simulated, respectively. The equilibration/measurement times are 2^x Monte Carlo sweeps.

Simulation path	L	N_{sa}	N_T	T_{min}	T_{max}	x
$h = 0.225$	8	1536	25	4.00	5.00	18
$h = 0.225$	10	827	25	4.00	5.00	18
$h = 0.225$	12	2048	17	4.30	4.80	18
$h = 0.225$	16	1024	19	4.35	4.70	18
$h = 0.225$	20	1024	19	4.35	4.70	18
$h = 0.225$	24	1024	26	4.40	4.69	18
$h = 0.225$	28	666	26	4.40	4.69	18
$h = 0.225$	32	406	26	4.40	4.69	18
$h = 0.225$	36	1017	26	4.40	4.69	18
$h = 0.5$	10	2503	17	4.20	4.60	18
$h = 0.5$	12	4035	17	4.20	4.60	18
$h = 0.5$	16	2048	17	4.20	4.60	18
$h = 0.5$	20	1024	14	4.30	4.50	18
$h = 0.5$	24	512	14	4.30	4.50	18
$h = 1.22T - 3.43$	10	4096	15	3.40	4.10	18
$h = 1.22T - 3.43$	12	3852	15	3.40	4.10	18
$h = 1.22T - 3.43$	16	1177	17	3.65	4.10	18
$h = 1.22T - 3.43$	18	862	17	3.65	4.10	18
$h = 1.22T - 3.43$	20	957	17	3.60	4.00	18
$h = 1.22T - 3.43$	24	976	17	3.60	4.00	18
$h = 1.22T - 3.43$	28	646	17	3.60	4.00	18
$h = 1.22T - 3.43$	32	379	17	3.60	4.00	18
$h = 2.67T - 6.10$	8	4071	25	2.80	3.06	18
$h = 2.67T - 6.10$	10	4045	25	2.80	3.06	18
$h = 2.67T - 6.10$	12	512	27	2.85	3.00	18
$h = 2.67T - 6.10$	14	512	27	2.85	3.00	18
$h = 2.67T - 6.10$	16	605	17	2.85	2.95	18
$h = 2.67T - 6.10$	18	1024	27	2.85	3.05	18
$h = 2.67T - 6.10$	20	512	31	2.86	2.93	18
$h = 2.67T - 6.10$	22	981	31	2.85	3.05	18
$h = 2.67T - 6.10$	24	1024	31	2.85	3.05	18
$h = 4.94T - 6.80$	16	1912	15	1.76	1.88	18
$h = 4.94T - 6.80$	18	2048	15	1.76	1.88	18
$h = 4.94T - 6.80$	20	1858	15	1.76	1.89	18
$h = 4.94T - 6.80$	24	906	15	1.76	1.89	18
$h = 4.94T - 6.80$	28	505	15	1.76	1.89	18
$h = 4.94T - 6.80$	32	627	15	1.76	1.89	18

Finally, we also study the DAFF at zero temperature using the method introduced in Refs. 33 and 34. Here, the DAFF is mapped onto a graph[35] with N nodes (N is the number of spins) attached to a source and a sink node, all connected in a distinct manner via edges with positive edge weights. The edge weights are calculated depending on the local staggered field, i.e., $\pm B$. The maximum flow/minimum cut is obtained using the algorithm introduced in Ref. 36. The minimum cut is

TABLE II. Simulation parameters for the DAFF along nontrivial paths of the type $B = a + bT$ in the B-T plane for different linear system sizes L (the first two path types have $b = 0$). N_{sa} is the number of disorder realizations. N_T corresponds to the number of temperatures (points) along the simulation path. $T_{\min}$ and $T_{\max}$ are the smallest and the highest temperatures of the RC, respectively. The equilibration/measurement times are 2^x Monte Carlo sweeps.

Simulation path	L	N_{sa}	N_T	$T_{\min}$	$T_{\max}$	x
$B = 0.1$	8	2166	26	2.50	3.50	18
$B = 0.1$	12	1208	26	2.50	3.50	18
$B = 0.1$	14	1042	18	2.70	3.30	18
$B = 0.1$	16	2048	19	2.80	3.30	18
$B = 0.1$	18	1104	19	2.80	3.30	18
$B = 0.1$	20	796	21	2.80	3.35	18
$B = 0.1$	24	444	21	2.80	3.35	18
$B = 0.1$	28	505	21	2.80	3.35	18
$B = 0.1$	32	322	21	2.80	3.35	18
$B = 1.0$	14	1271	21	2.70	3.20	18
$B = 1.0$	16	1718	21	2.70	3.20	18
$B = 1.0$	18	1215	21	2.70	3.20	18
$B = 1.0$	20	888	21	2.70	3.20	18
$B = 1.0$	24	491	21	2.70	3.20	18
$B = 1.0$	28	556	21	2.70	3.20	18
$B = 1.0$	32	352	21	2.70	3.20	18
$B = 0.2T$	8	1344	17	2.55	3.30	18
$B = 0.2T$	10	685	17	2.55	3.30	18
$B = 0.2T$	12	452	17	2.55	3.30	18
$B = 0.2T$	16	542	31	2.87	3.50	18
$B = 0.2T$	20	1564	31	2.87	3.50	18
$B = 0.2T$	22	825	31	2.87	3.50	18
$B = 0.2T$	24	189	31	2.87	3.50	18
$B = 0.2T$	26	128	31	2.87	3.50	18
$B = 0.2T$	28	115	31	2.87	3.50	18
$B = 0.2T$	30	558	31	2.87	3.50	18
$B = 0.2T$	32	383	31	2.87	3.50	18
$B = 0.67T$	10	1201	30	2.45	3.50	18
$B = 0.67T$	12	711	30	2.45	3.50	18
$B = 0.67T$	16	305	30	2.45	3.50	18
$B = 0.67T$	20	512	27	2.35	3.50	18
$B = 0.67T$	22	1024	27	2.35	3.50	18
$B = 0.67T$	24	2048	30	2.35	3.50	18
$B = 0.67T$	28	1024	27	2.35	3.50	18
$B = 0.67T$	32	741	30	2.37	3.50	18
$B = 1.5T$	10	1920	17	1.30	1.62	18
$B = 1.5T$	12	1984	17	1.30	1.62	18
$B = 1.5T$	16	2048	17	1.30	1.62	18
$B = 1.5T$	18	2048	26	1.30	3.50	18
$B = 1.5T$	20	1056	20	1.35	1.60	18
$B = 1.5T$	24	807	20	1.35	1.60	18
$B = 1.5T$	28	457	20	1.35	1.60	18
$B = 1.5T$	32	532	20	1.35	1.60	18
$B = 1.5T$	36	336	20	1.35	1.60	18

a direct representation of the ground-state spin configuration from which derived quantities, such as a zero-temperature Binder ratio, can be calculated. Note that the method takes the ground-state degeneracy into account. The simulation parameters for the DAFF at zero temperature are shown in Table III.

TABLE III. Simulation parameters for the DAFF at zero temperature for different fields B and for different linear system sizes L. N_{sa} is the number of disorder realizations. $B_{\min}$ and $B_{\max}$ are the lowest and highest fields simulated, and N_B corresponds to the number of fields simulated to perform a finite-size scaling analysis.

L	N_{sa}	$B_{\min}$	$B_{\max}$	N_B
24	10302	2.00	4.30	31
32	2091	2.40	2.70	16
48	2091	2.10	2.80	17
64	2091	2.30	2.70	21
72	2040	2.30	2.54	17
96	5100	2.30	2.54	17
128	3586	2.30	2.47	22

IV. OBSERVABLES

Both the DAFF and RFIM undergo second-order phase transitions as a function of temperature and field. To pinpoint the transition temperature, we measure the Binder cumulant,[37] as well as the two-point finite-size correlation function.[38–40] To compute these observables, we measure the magnetization per spin

$$M = \frac{1}{N}\sum_{i}^{N} S_i. \tag{6}$$

For the DAFF we measure the *staggered* magnetization, i.e., each second spin is counted opposite to its orientation in a three-dimensional checker-board manner. For simplicity, we refer to the staggered magnetization also as M. An antiferromagnetically-ordered spin configuration has therefore $M = 1$. A Binder cumulant for M can then be defined via

$$g(T,L) = \frac{1}{2}\left(3 - \frac{[\langle M^4\rangle]_{\text{av}}}{[\langle M^2\rangle^2]_{\text{av}}}\right), \tag{7}$$

where $\langle\cdots\rangle$ represents a thermal average and $[\cdots]_{\text{av}}$ an average over disorder (field or dilution configurations) for a fixed value of h (RFIM) or B (DAFF). Close to criticality the Binder ratio scales as

$$g(T,L) = \tilde{G}[L^{1/\nu}(T - T_c)], \tag{8}$$

where $\tilde{G}$ is a universal function. Note that for the DAFF, when $T = 0$, $g(B,L) = \tilde{G}'[L^{1/\nu}(B - B_c)]$. To compute the two-point finite-size correlation function we first calculate the wave-vector-dependent susceptibility (along the x direction) via

$$\chi(\mathbf{k}) = \left[\left\langle\left(\frac{1}{N}\sum_{j} S_j e^{ikx_j}\right)^2\right\rangle\right]_{\text{av}}. \tag{9}$$

The two-point finite-size correlation function is then given by

$$\xi_L = \frac{1}{2\sin(k_{\min}/2)}\sqrt{\frac{\chi(\mathbf{0})}{\chi(\mathbf{k}_{\min})} - 1} \tag{10}$$

with $\mathbf{k}_{\min} = (2\pi/L,0,0)$. The two-point finite-size correlation function scales as

$$\xi_L(T,L)/L = \tilde{X}[L^{1/\nu}(T - T_c)]. \tag{11}$$

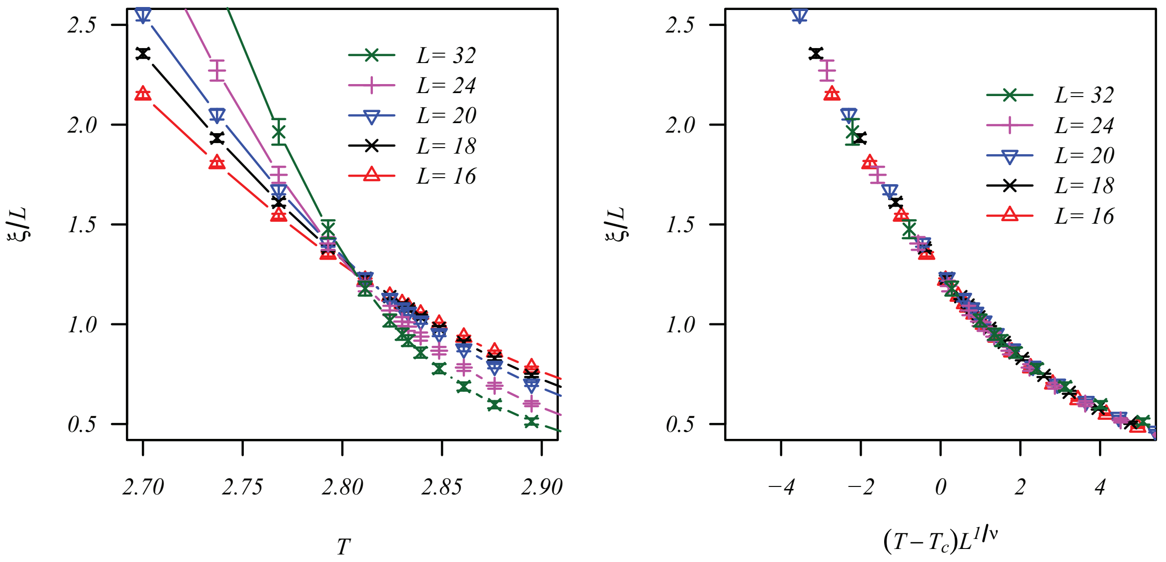

FIG. 1. (Color online) Left: Two-point finite-size correlation function ξ_L/L vs temperature T for the DAFF with $B = 1.0$ and different linear system sizes L. Finite-size corrections are small and the data cross at one point signaling a transition. Right: Finite-size scaling collapse of the data in the left panel. The best collapse is obtained with $T_c \approx 2.807$ and $\nu \approx 1.2$.

Using both the Binder ratio and the two-point finite-size correlation function allows us to perform a detailed finite-size scaling analysis to determine the critical exponent ν, as well as to test if both models share the same universality class using the method introduced in Ref. 41. To obtain an optimal data collapse we use a Levenberg-Marquardt minimization combined with a bootstrap analysis, see Ref. 41. This allows us to determine the optimal values of the critical parameters T_c and ν with a statistical error bar by fitting the data to a third-order polynomial that approximates the scaling functions $\tilde{G}(x)$ and $\tilde{X}(x)$ close to $x = 0$, where $x = L^{1/\nu}(T - T_c)$.

Finally, to determine the critical exponent η, we determine the peak position of the connected susceptibility given by

$$\chi = \frac{1}{T}\left([\langle M^2\rangle]_{\rm av} - [\langle M\rangle]_{\rm av}^2\right), \qquad (12)$$

where the magnetization M is given by Eq. (6). Note that the connected susceptibility is related to Eq. (9) in the limit of zero wave vector. Furthermore, in the thermodynamic limit $[\langle M\rangle]_{\rm av} = 0$ for $T = T_c$ so, in principle, Eq. (9) could also be used for the analysis. In general, the susceptibility scales as

$$\chi \sim L^{2-\eta}\widetilde{C}[L^{1/\nu}(T - T_c)]\,. \qquad (13)$$

Therefore, when $T = T_c$ the function $\widetilde{C}$ is a constant independent of the system size and $\chi \sim L^{2-\eta}$ from which the exponent η can be determined.

V. RESULTS

The critical parameters for both the RFIM and the DAFF have been computed via a finite-size scaling analysis of the two-point finite-size correlation function [Eq. (11)] along the different simulation paths. Finite-size corrections can be large for small system sizes and are strongly field dependent, which is why for some external fields in both models we do not include small systems in the finite-size scaling analysis used to determine the critical parameters. To illustrate the typical behavior, in Fig. 1, left panel, we show the two-point finite-size correlation function for the DAFF for $B = 1.0$ and different system sizes. The data cross at a point, therefore signaling the existence of a phase transition. Note that for this particular field corrections to scaling are manageable and the data scale well, as can be seen in Fig. 1, right panel. However, this is not always the case, especially when the external field is large. For the RFIM corrections to scaling are considerably stronger, even at small fields, see Fig. 2.

Using finite-size scaling we determine the location of the critical points, as well as the associated critical exponent ν for the different simulation paths. In addition, we also compute the critical exponent η by studying the finite-size behavior of the susceptibility peak. Data for the RFIM are summarized in Table IV, for the DAFF in Table V.

To determine the critical field B_c at zero temperature for the DAFF we compute ground states with the algorithm introduced in Ref. 34. The same finite-size scaling technique as used for the two-point finite-size correlation function (see above) can be used to analyze the ground-state Binder cumulant. The data collapse is shown in Fig. 3. The results for the critical point and the correlation-length exponent at zero temperature are stated in the last line of Table V.

TABLE IV. Critical temperature T_c and critical field h_c computed from a finite-size scaling analysis of the two-point finite-size correlation function for the RFIM. ν is the critical exponent of the correlation length. The exponent η is computed from the peak of the susceptibility.

Simulation path	T_c	h_c	ν	η
$h = 0.225$	4.481(1)	0.225	1.39(4)	0.082(1)
$h = 0.5$	4.381(2)	0.5	1.30(5)	0.202(16)
$h = 1.22T - 3.4$	3.76(2)	1.16(3)	1.39(5)	0.92(40)
$h = 2.70T - 6.1$	2.89(5)	1.7(1)	1.3(1)	0.47(15)
$h = 4.94T - 6.8$	1.79(1)	2.01(5)	1.4(1)	0.85(4)

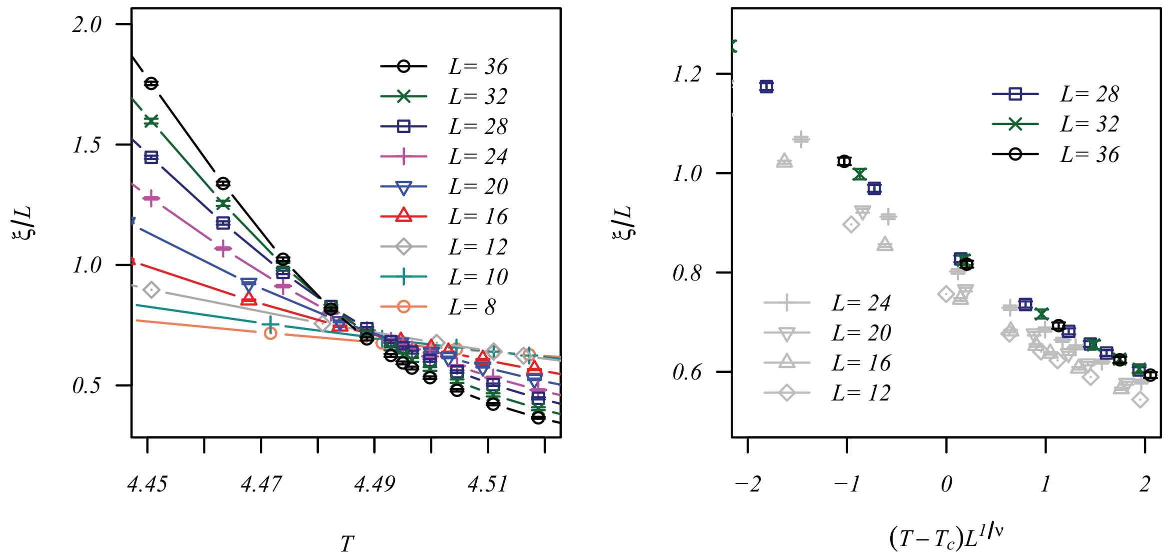

FIG. 2. (Color online) Left: Two-point finite-size correlation function ξ_L/L vs temperature T for the RFIM with $h = 0.225$ and different linear system sizes L. Finite-size corrections are large. Right: Finite-size scaling collapse of the data in the left panel. Because of the large corrections to scaling, only data for $L \geqslant 28$ are used in the scaling collapse. Data for $L \leqslant 24$ (light shaded) are not included in the data collapse and shown to illustrate the corrections to scaling. The best collapse is obtained with $T_c \approx 4.481$ and $\nu \approx 1.39$.

We also determine the peak position of the fluctuations of the staggered magnetization of the ground states:

$$\mathcal{F}(B) = L^3\left([M^2]_{\rm av} - [M]^2_{\rm av}\right). \tag{14}$$

This approach has proven to be quite accurate in previous studies for the susceptibility.[42] Because the fluctuations peak at the putative transition, we fit a Gaussian to the peak and determine its precise location. Error bars are determined via a configurational bootstrap analysis.[43] Figure 4, left panel, shows the fluctuations at zero temperature and as a function of the applied field B. The peaks are well described by Gaussians. The right panel of Fig. 4 shows an extrapolation of the peak position to infinite system size assuming the functional form $B_c(L) = B_c + aL^{-\omega}$. The best fit is obtained for $B_c = 2.34(2)$ [$\omega = 1.25(9)$], in agreement with the estimate using the Binder cumulant, see Table V.

Combining the data in Table V with some values from the literature[44–47] we can approximate to good accuracy the phase boundary for the DAFF via

$$\left(\frac{B_c}{\tilde{B}_c^0}\right)^{1.81} + \left(\frac{T_c}{\tilde{T}_c^0}\right)^{3.54} = 1 \tag{15}$$

with $\tilde{T}_c^0 \approx 2.980$ and $\tilde{B}_c^0 \approx 2.31$. Similarly, using the data from Table IV and known values from the literature[48–50] we obtain for the RFIM

$$\left(\frac{h_c}{h_c^0}\right)^{1.95} + \left(\frac{T_c}{T_c^0}\right)^{1.80} = 1 \tag{16}$$

TABLE V. Critical temperature T_c and critical field B_c computed from a finite-size scaling analysis of the two-point finite-size correlation function for the DAFF. ν is the critical exponent of the correlation length. The exponent η is computed from the peak of the susceptibility. Note that estimating η was not possible for $B = 1.5$. The last line lists data from zero-temperature simulations (see text). The estimate of the critical field B_c is obtained from a finite-size scaling analysis of the zero-temperature Binder ratio.

Simulation path	T_c	B_c	ν	η
$B = 0.1$	2.977(1)	0.1	1.34(5)	0.406(26)
$B = 1.0$	2.807(1)	1.0	1.2(2)	0.023(12)
$B = 0.2T$	2.908(4)	0.582(8)	1.36(7)	0.11(2)
$B = 0.67T$	2.42(1)	1.61(1)	1.5(3)	0.67(5)
$B = 1.5$	1.46(9)	2.2(1)	1.4(3)	
$T = 0$	0	2.32(2)	1.43(2)	0.68(1)

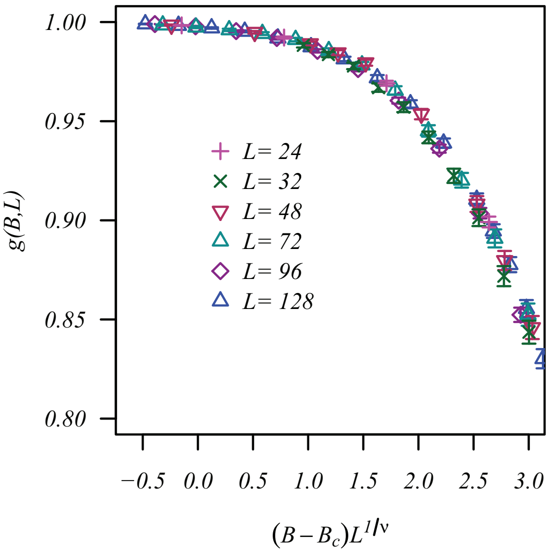

FIG. 3. (Color online) Data collapse of the zero-temperature Binder cumulant of the DAFF as a function of the reduced scaling variable $(B - B_c)L^{1/\nu}$ for different system sizes. The best collapse is obtained for $B_c^0 \approx 2.32$ and $\nu \approx 1.43$.

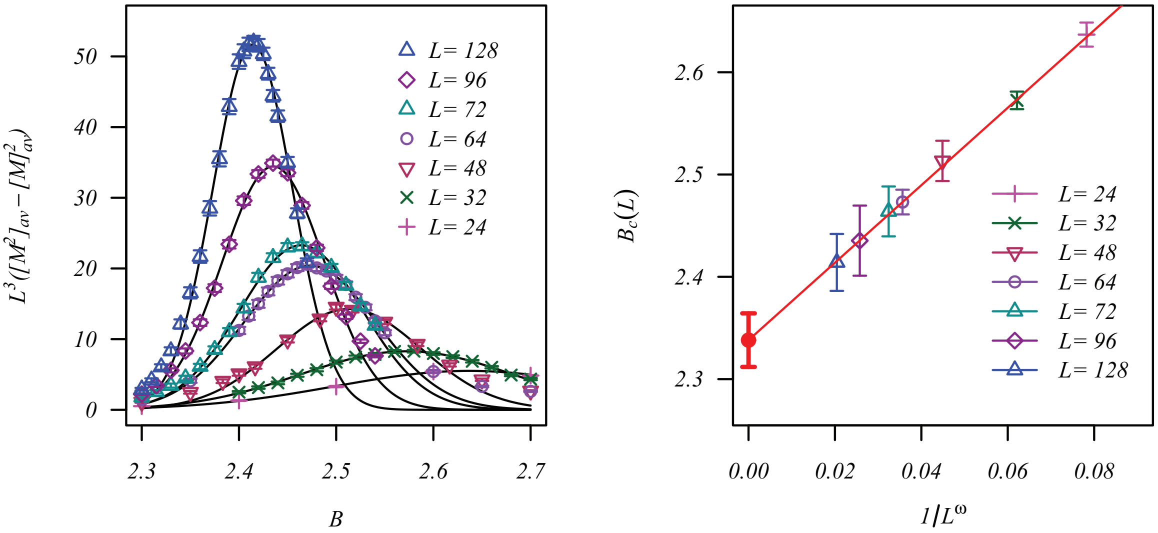

FIG. 4. (Color online) Left: Fluctuations of the staggered magnetization of the DAFF as a function of applied field B for different system sizes. The peak positions signals the presence of a transition. The data are well described by a Gaussian close to the peak (solid lines). To determine the thermodynamic critical field B_c we extrapolate the data to infinite system size (right panel) using $B_c(L) = B_c + aL^{-\omega}$. The best fit is obtained for $B_c = 2.34(2)$ and $\omega = 1.25(9)$. The red (filled) point represents the thermodynamic extrapolation, $B_c = 2.34(2)$.

with $h_c^0 = 2.27$[49] and $T_c^0 = 4.5115$.[48] Note that the critical phase boundary points T_c^0 and h_c^0 have been determined to high precision in the literature; see Refs. 48 and 49, respectively. Furthermore, for the RFIM with bimodal disorder, a similar elliptical phase diagram has been proposed in Ref. 51. For the DAFF, $\tilde{T}_c^0$ and $\tilde{B}_c^0$ are approximated but agree with the numerical estimates we present. In Fig. 5 we show the phase boundaries for the DAFF (left panel) and the RFIM (right panel), together with the simulated critical points. The dashed lines represent the simulation paths taken.

VI. DISCUSSION

Cardy[17] predicted an equivalence between the DAFF and the RFIM for small applied fields using a mean-field argument. This equivalence is often quoted in experimental studies where materials which are diluted antiferromagnets in a field are

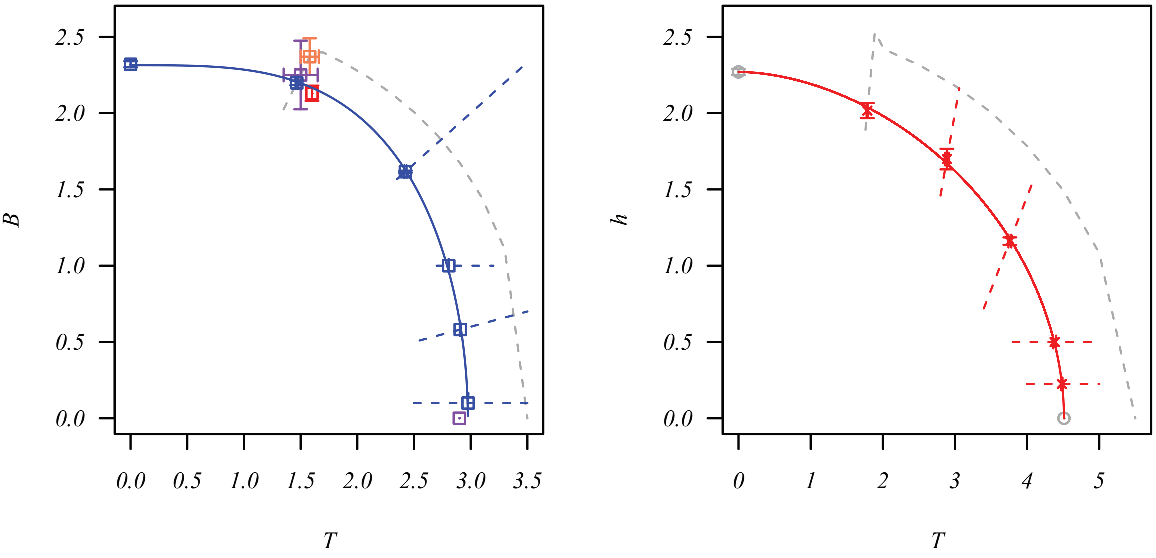

FIG. 5. (Color online) Left: Empirical phase boundary of the DAFF ($p = 0.7$). The red point is from Ref. 44, the coral point from Ref. 45, and the purple points from Ref. 46. Our data agree within error bars with these previous studies. The blue (solid) curve is given by Eq. (15). The dashed lines represent the parts of the simulation paths that cross the phase boundary. The light shaded line is an example of the second RC that runs parallel to the approximated phase boundary to a temperature $T > T_c$ and $B = 0$ to speed up equilibration. Right: Empirical phase boundary of the RFIM. The zero-field critical temperature is $T_c^0 = 4.5115$[48] and $h_c^0 = 2.270$[49] (gray open circles). The red (solid) curve is given by Eq. (16). The dashed lines represent the parts of the simulation paths that cross the phase boundary. Again, the light shaded line shows an example of the second RC that runs parallel to the approximated phase boundary to a temperature $T > T_c$ and $h = 0$ to speed up equilibration.

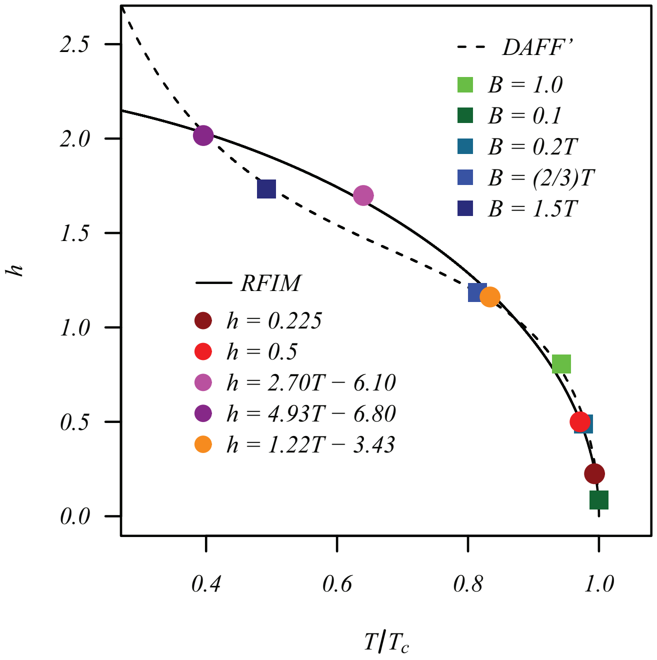

FIG. 6. (Color online) Phase boundary of the RFIM (solid line, from Fig. 5, right panel). The temperature axis has been normalized with $T_c(h = 0) = 4.5115$. The circles represent the different estimates of the critical points along the different simulation paths. The dashed line is the phase boundary computed by applying Eq. (17) to the data of the DAFF. Squares represent the different critical points simulated for the DAFF along the different simulation paths. An approximate correspondence between the phase boundaries only works for fields $h \lesssim 1.2$ ($B \lesssim 1.6$ for the DAFF).

then described using the RFIM (see, for example, Refs. 3 and 12–15).

Equation (15) in Ref. 17 maps the RFIM onto the DAFF:

$$h(T) = \frac{p(1-p)\left(T_c^{\text{pure}}/T\right)^2(B/T)^2}{(1-\theta^{MF}/T)^2}. \tag{17}$$

Here, $p = 0.7$, $T_c^{\text{pure}} = 4.5115$, and $\theta^{MF} = 2dJ = 6$ is the mean-field coupling strength. We can now use the obtained phase boundaries [Eqs. (15) and (16)] to compare both models. Figure 6 shows the phase boundary for the RFIM (solid line, the circles represent the obtained critical points along the different simulation paths) together with the phase boundary for the DAFF mapped onto the RFIM space using Eq. (17) (dashed line, the squares represent the obtained critical points along the different simulation paths for the DAFF). For random-field strengths of up to $h \approx 1.2$—which means field strengths of up to $B \approx 1.6$ for the DAFF—there is an approximate correspondence between both models. However, as the figure clearly illustrates, strictly speaking the correspondence only seems to work in the limit of $h \to 0$ ($h \lesssim 0.3$). Given the mean-field nature of the Cardy argument, the agreement of the phase boundaries is rather good. On the other hand, it is not surprising that for larger disorder, they do not agree exactly. It is of importance to take these limitations of the Cardy mapping[17] into account when studying diluted antiferromagnets in an external field experimentally while attempting to describe the data analytically using the RFIM.

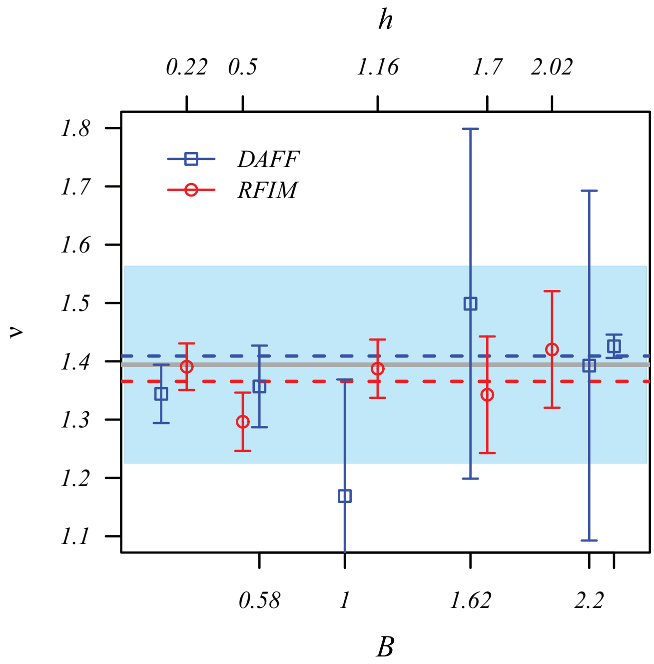

FIG. 7. (Color online) Critical exponent ν as a function of the field h (RFIM) and B (DAFF). The labels on the upper axis correspond to the random-field strength h (RFIM), those on the lower axis to the external field B (DAFF). The weighted mean is $\nu = 1.39(17)$ (gray line) and the weighted error is represented by the shaded (light blue) area. The difference between $\bar{\nu}_{\text{DAFF}} = 1.41(15)$ (blue dashed line) and $\bar{\nu}_{\text{RFIM}} = 1.37(12)$ (red dashed line) is marginal in comparison to the error bars of the data points. The RFIM ground-state value is taken from Ref. 49.

Furthermore, a basic finite-size scaling analysis leads to no systematic deviations of the correlation-length exponent ν. Including the estimates for rough simulations at high fields, our results support

$$\nu = 1.39(17) \tag{18}$$

for the range of fields studied, in agreement with previous studies, such as $\nu_{\text{RFIM}} = 1.37(9)$,[49] $\nu = 1.20(5)$[14] from experiments on $\text{Fe}_{0.85}\text{Zn}_{0.15}\text{F}_2$ ($p = 0.85$), or $\nu = 1.40(6)$ from the disconnected part of the susceptibility of $\text{Fe}_{0.93}\text{Zn}_{0.07}\text{F}_2$ ($p = 0.93$).[52] Note that our results are also compatible with the value $\nu = 1.10(15)$ computed by Fernandez *et al.*[44] obtained for their largest system size using the quotient method. They do find other values of ν for smaller system sizes. Our results are summarized in Fig. 7. As can be clearly seen, the difference between the estimates for the critical exponent of the correlation length for both models is marginal and within error bars: The *average* estimate for the RFIM is $\bar{\nu}_{\text{RFIM}} = 1.37(12)$ (red line in Fig. 7), whereas for the DAFF $\bar{\nu}_{\text{DAFF}} = 1.41(15)$ (blue line in Fig. 7). This apparent agreement of the critical exponent is quite good, given that the proposed equivalence is based on a mean-field argument that typically leads to quite different exponents compared to the true non-mean-field values.

However, the error bars are large and therefore a more detailed study needs to be performed. To truly discern if both models are in the same universality class, in addition to having one (apparently) agreeing critical exponent, one would have

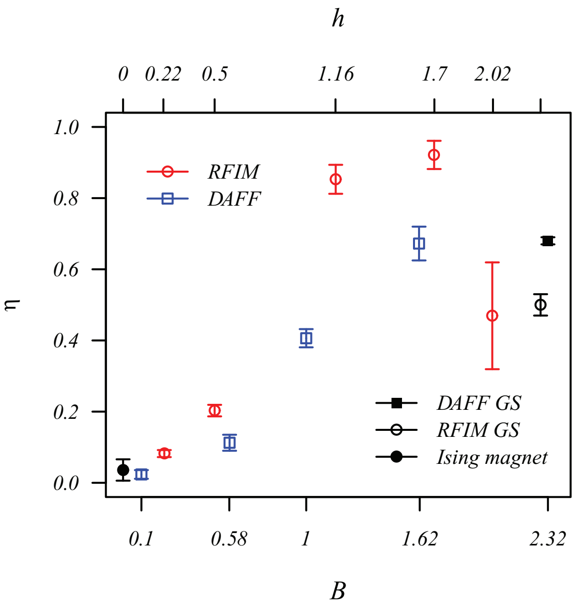

FIG. 8. (Color online) Critical exponent η as a function of the field h (RFIM) and B (DAFF). The labels on the upper axis correspond to the random-field strength h (RFIM), those on the lower axis to the external field B (DAFF). For comparison, we also add the estimates for the three-dimensional Ising ferromagnet (filled circle at $h = 0$, marked with "Ising magnet"),[48] the RFIM at $T = 0$ (open circle at $h = h_c$, marked with "RFIM GS"),[50] and the DAFF at $T = 0$ and $B = B_c$ computed from our ground-state data [$\eta(T = 0) \approx 0.68(1)$, filled square, marked with "DAFF GS"]. Note that we find very large fluctuations, i.e., a detailed determination of the different universality classes is difficult.

to compute a second critical exponent. We also analyzed the behavior of the magnetic susceptibility χ which has a peak at the phase transition. By studying the finite-size behavior of the peak height (not shown), we determine the critical exponent η using the finite-size scaling form of the susceptibility, Eq. (13). Our estimates of the critical exponent η along the phase boundary are shown in Fig. 8 and summarized in Tables IV and V for the RFIM and DAFF, respectively. Fluctuations are very large, especially for large fields, but suggest that both the RFIM and the DAFF might not share the same universality class. For the DAFF, a clear systematic trend is visible that shows that η might be strongly field dependent for $B \gtrsim 1.6$, i.e., in the curved portion of the phase boundary. However, note that the exponent η is very difficult to compute, as recently shown in Ref. 20. A different approach is the computation of the critical exponent α that describes the divergence of the specific heat. However, for both the RFIM and the DAFF α is close to zero.[34,49] Therefore, simulations of very large system sizes that are currently not accessible numerically are required.

Fortunately, there is a simple yet more sensitive method to verify if two different systems share the same universality class without having to compute any critical exponents:[41,53] Both the Binder cumulant and the two-point finite-size correlation function divided by the system size are dimensionless quantities. By plotting one as a function of the other, nonuniversal quantities cancel out.[41] For a given system, once large enough system sizes are reached such that corrections to scaling are negligible, the data for all system sizes collapse onto a universal curve within error bars. If two systems share the same critical exponent ν, we expect that all data should collapse onto the same universal curve within error bars and, in particular, that the estimates of the Binder cumulant and the two-point finite-size correlation function agree at the putative critical point(s). We therefore would expect that data sets of $g(\xi_L/L)$ for both the DAFF and the RFIM should agree for all simulated temperatures and, in particular, for $T = T_c$.

Figure 9 shows the Binder cumulant as a function of the two-point finite-size correlation function divided by the system size for both the DAFF and the RFIM. The left set of points (reddish/light tones, circles) are for the RFIM. Data for the different simulation paths used collapse onto a master curve. The right set of points (greenish/dark tones, squares) are for the DAFF. Again, all data collapse onto a master curve for all simulation paths taken. This shows that for this type of analysis the finite-size corrections are small for both models and within the statistical fluctuations. However, the data sets for the RFIM and the DAFF do not agree, except in the trivial limit where $g(T) \to 1$. The large circles for the RFIM (squares for the DAFF) represent our estimates of $g(\xi_L/L)$ at $T = T_c$. As can be seen, the data for both models do not agree (i.e., a large circle should sit on top of a large square), something which is even more clear when zooming into the boxed area (inset). Note that the large error bars are due to the uncertainty of the critical temperature. This discrepancy reveals the differences between the DAFF and the RFIM which could not be detected within the scope of a mean-field calculation.

VII. CONCLUSIONS

We have performed extensive Monte Carlo simulations of the diluted antiferromagnet in a field at 30% dilution ($p = 0.7$) and the random-field Ising model. Using these data we show that the phase boundaries for both models are well described by ellipses (see Fig. 5). In addition, using zero-temperature heuristic methods, we compute the zero-temperature critical point for the DAFF with 30% dilution ($p = 0.7$). We expect that the phase boundary for other dilutions will be similar, albeit with different nonuniversal parameters. Furthermore, we numerically study the equivalence of the RFIM and the DAFF as predicted by Cardy.[17] Our results show that only in the limit of small fields do both phase boundaries map onto each other.

Finally, we perform a finite-size scaling analysis to determine the critical exponent ν of the correlation length. Our results from the two-point finite-size correlation function suggest that the exponent ν agrees within error bars for both the RFIM and the DAFF. However, error bars are large. To circumvent this problem, we study the Binder cumulant as a function of the two-point finite-size correlation function divided by the system size and show that both models apparently do not share the same universality class. A computation of the exponent η is extremely difficult and plagued by finite-size effects. Clearly, more detailed simulations need to be performed to fully discern the critical behavior of both models and fully determine their universality classes. It would be interesting to also measure the critical behavior of the specific heat (critical exponent α). However, because the exponent is close to zero for both

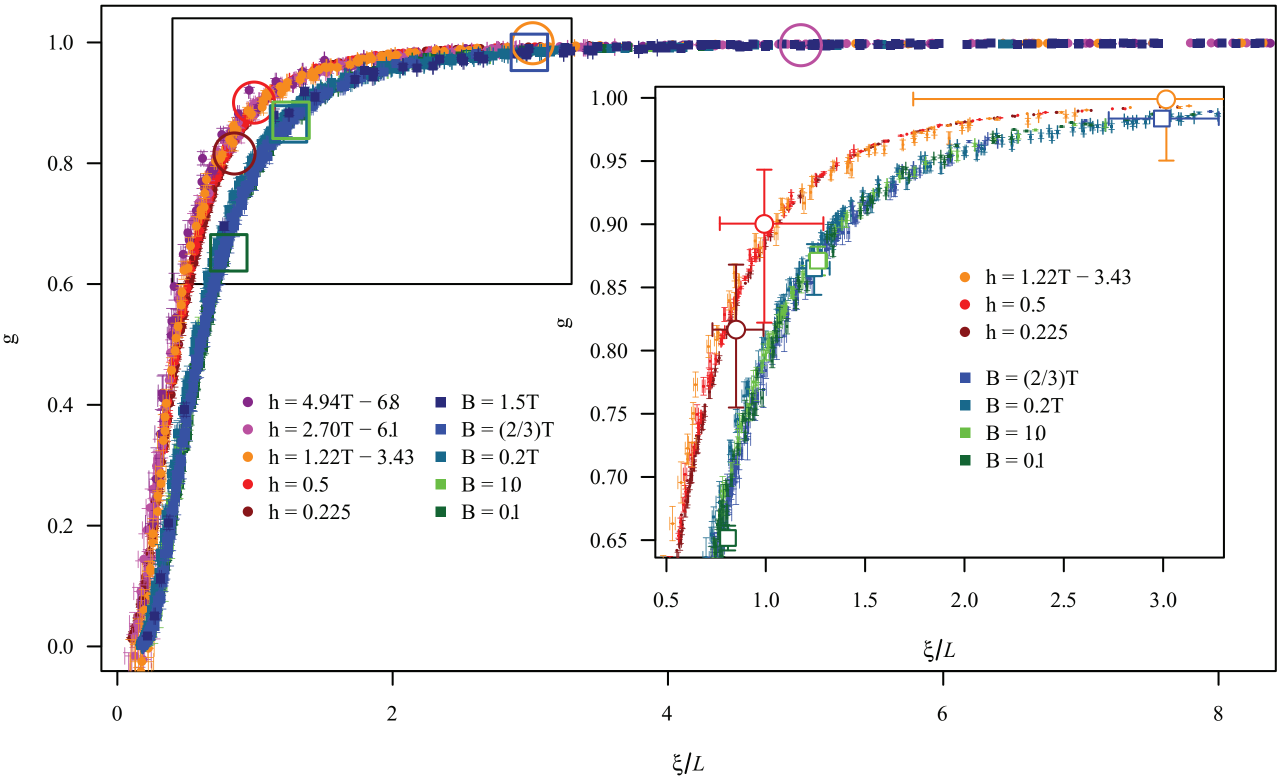

FIG. 9. (Color online) Binder ratio g as a function of the two-point finite-size correlation function divided by the system size ξ_L/L for several system sizes and simulation paths. Note that also small system sizes are included, i.e., corrections to finite-size scaling are small. The data for the RFIM and DAFF collapse onto two distinct set of curves, suggesting that both models do not share the same universality class. The left set of points (reddish/light tones, circles) are for the RFIM. The right set of points (greenish/dark tones, squares) are for the DAFF. The large circles for the RFIM (large squares for the DAFF) represent our estimates of $g(\xi_L/L)$ at $T = T_c$. The inset zooms into the important region (large box), where the Cardy mapping should apply. Clearly, both data sets are different, suggesting that the RFIM and the DAFF do not share the same universality class.

models, large system sizes are needed; sizes that are currently not accessible via simulations. We conclude by cautioning researchers when using the equivalence of both models.

ACKNOWLEDGMENTS

We would like to thank D. P. Belanger, M. Niemann, and A. P. Young for the fruitful discussions. H.G.K. acknowledges support from the SNF (Grant No. PP002-114713) and the NSF (Grant No. DMR-1151387). We would like to thank ETH Zurich for CPU time on the Brutus cluster, Texas A&M University for CPU time on the Eos cluster, as well as the C. v. O. Universität Oldenburg for CPU time on the Hero cluster funded by the DFG (INST 184/108-1 FUGG) and the ministry of Science and Culture (MWK) of the Lower Saxony State.

---

[1] D. P. Belanger and A. P. Young, J. Magn. Magn. Mater. **100**, 272 (1991).
[2] T. Nattermann, J. Phys. A **21**, L645 (1988).
[3] D. P. Belanger, *Experiments on the random field Ising model*, in *Spin Glasses and Random Fields*, edited by A. P. Young (World Scientific, Singapore, 1998), p. 251.
[4] T. Nattermann, *Theory of the random field Ising model*, in *Spin Glasses and Random Fields*, edited by A. P. Young (World Scientific, Singapore, 1998), p. 277.
[5] I. F. Lyuksyutov, T. Nattermann, and V. Pokrovsky, Phys. Rev. B **59**, 4260 (1999).
[6] *Spin Glasses and Random Fields*, edited by A. P. Young (World Scientific, Singapore, 1998).
[7] J. P. Sethna, K. Dahmen, S. Kartha, J. A. Krumhansl, B. W. Roberts, and J. D. Shore, Phys. Rev. Lett. **70**, 3347 (1993).
[8] O. Perkovic, K. A. Dahmen, and J. P. Sethna, Phys. Rev. Lett. **75**, 4528 (1995).
[9] O. Perkovic, K. A. Dahmen, and J. P. Sethna, Phys. Rev. B **59**, 6106 (1999).
[10] D. M. Silevitch, G. Aeppli, and T. F. Rosenbaum, Proc. Natl. Acad. Sci. USA **107**, 2797 (2010).
[11] T. Halpin-Healy, Phys. Rev. A **44**, R3415 (1991).
[12] W. Barber and D. Belanger, J. Appl. Phys. **87**, 7049 (2000).
[13] F. Ye, L. Zhou, S. Larochelle, L. Lu, D. P. Belanger, M. Greven, and D. Lederman, Phys. Rev. Lett. **89**, 157202 (2002).

[14] F. Ye, M. Matsuda, S. Katano, H. Yoshizawa, D. P. Belanger, E. T. Seppälä, J. A. Fernandez-Baca, and M. J. Alava, JMMM **272**, 1298 (2004).

[15] F. Ye, L. Zhou, S. A. Meyer, L. J. Shelton, D. P. Belanger, L. Lu, S. Larochelle, and M. Greven, Phys. Rev. B **74**, 144431 (2006).

[16] S. Fishman and A. Aharony, J. Phys. C **12**, L729 (1979).

[17] J. L. Cardy, Phys. Rev. B **29**, 505 (1984).

[18] N. Sourlas, Comput. Phys. Commun. **121**, 183 (1999).

[19] A. K. Hartmann and U. Nowak, Eur. Phys. J. B **7**, 105 (1999).

[20] N. G. Fytas and V. Martin-Mayor, Phys. Rev. Lett. **110**, 227201 (2013).

[21] J. Machta, M. E. J. Newman, and L. B. Chayes, Phys. Rev. E **62**, 8782 (2000).

[22] M. E. J. Newman and G. T. Barkema, *Monte Carlo Methods in Statistical Physics* (Oxford University Press Inc., New York, 1999).

[23] H. G. Katzgraber, arXiv:0905.1629 (2009).

[24] R. H. Swendsen and J.-S. Wang, Phys. Rev. Lett. **57**, 2607 (1986).

[25] C. Geyer, in *23rd Symposium on the Interface*, edited by E. M. Keramidas (Interface Foundation, Fairfax Station, VA, 1991), p. 156.

[26] E. Marinari and G. Parisi, Europhys. Lett. **19**, 451 (1992).

[27] J. J. Moreno, H. G. Katzgraber, and A. K. Hartmann, Int. J. Mod. Phys. C **14**, 285 (2003).

[28] A. P. Young and H. G. Katzgraber, Phys. Rev. Lett. **93**, 207203 (2004).

[29] Note that Ref. 21 contains a mistake regarding the definition of n_{++} and n_{--}.

[30] N. B. Wilding and A. D. Bruce, J. Phys.: Condens. Matter **4**, 3087 (1992).

[31] T. Jörg, H. G. Katzgraber, and F. Krzakala, Phys. Rev. Lett. **100**, 197202 (2008).

[32] U. Wolff, Phys. Rev. Lett. **62**, 361 (1989).

[33] J. Esser, U. Nowak, and K. D. Usadel, Phys. Rev. B **55**, 5866 (1997).

[34] A. K. Hartmann, Physica A **248**, 1 (1998).

[35] J. C. Picard and H. D. Ratliff, Networks **5**, 357 (1975).

[36] A. V. Goldberg and R. E. Tarjan, J. ACM **35**, 921 (1988).

[37] K. Binder, Z. Phys. B **43**, 119 (1981).

[38] F. Cooper, B. Freedman, and D. Preston, Nucl. Phys. B **210**, 210 (1982).

[39] H. G. Ballesteros, A. Cruz, L. A. Fernández, V. Martín-Mayor, J. Pech, J. J. Ruiz-Lorenzo, A. Tarancón, P. Téllez, C. L. Ullod, and C. Ungil, Phys. Rev. B **62**, 14237 (2000).

[40] M. Palassini and S. Caracciolo, Phys. Rev. Lett. **82**, 5128 (1999).

[41] H. G. Katzgraber, M. Körner, and A. P. Young, Phys. Rev. B **73**, 224432 (2006).

[42] B. Ahrens and A. K. Hartmann, Phys. Rev. B **83**, 014205 (2011).

[43] A. K. Hartmann, *Practical Guide to Computer Simulations* (World Scientific, Singapore, 2009).

[44] L. A. Fernandez, V. Martin-Mayor, and D. Yllanes, Phys. Rev. B **84**, 100408 (2011).

[45] A. Maiorano, V. Martin-Mayor, J. J. Ruiz-Lorenzo, and A. Tarancón, Phys. Rev. B **76**, 064435 (2007).

[46] A. T. Ogielski and D. A. Huse, Phys. Rev. Lett. **56**, 1298 (1986).

[47] D. Yllanes, Ph.D. thesis, Universidad Complutense de Madrid, 2011, arXiv:1111.0266 [cond-mat.dis-nn].

[48] A. L. Talapov and H. W. J. Blöte, J. Phys. A **29**, 5727 (1996).

[49] A. A. Middleton and D. S. Fisher, Phys. Rev. B **65**, 134411 (2002).

[50] A. K. Hartmann and A. P. Young, Phys. Rev. B **64**, 214419 (2001).

[51] N. G. Fytas and A. Malakis, Eur. Phys. J. B **61**, 111 (2008).

[52] Z. Slanic, D. P. Belanger, and J. A. Fernandez-Baca, J. Phys.: Condens. Matter **13**, 1711 (2001).

[53] T. Jörg, Phys. Rev. B **73**, 224431 (2006).